5-10-2012

Monitoring Glacier Surface Seismicity in Time and Space Using Rayleigh Waves

T. D. Mikesell
Université de Nice Sophia-Antipolis

Kasper van Wijk
Boise State University

Matthew M. Haney
Boise State University

John H. Bradford
Boise State University

Hans-Peter Marshall
Boise State University

See next page for additional authors

Authors

T. D. Mikesell, Kasper van Wijk, Matthew M. Haney, John H. Bradford, Hans-Peter Marshall, and Joel T. Harper

Monitoring glacier surface seismicity in time and space using Rayleigh waves

T. D. Mikesell,[1,2] K. van Wijk,[3] M. M. Haney,[2,4] J. H. Bradford,[3] H. P. Marshall,[3] and J. T. Harper[5]

[1]   Sliding glaciers and brittle ice failure generate seismic body and surface wave energy characteristic to the source mechanism. Here we analyze continuous seismic recordings from an array of nine short-period passive seismometers located on Bench Glacier, Alaska (USA) (61.033°N, 145.687°W). We focus on the arrival-time and amplitude information of the dominant Rayleigh wave phase. Over a 46-hour period we detect thousands of events using a cross-correlation based event identification method. Travel-time inversion of a subset of events (7% of the total) defines an active crevasse, propagating more than 200 meters in three hours. From the Rayleigh wave amplitudes, we estimate the amount of volumetric opening along the crevasse as well as an average bulk attenuation ($\bar{Q} = 42$) for the ice in this part of the glacier. With the remaining icequake signals we establish a diurnal periodicity in seismicity, indicating that surface run-off and subglacial water pressure changes likely control the triggering of these surface events. Furthermore, we find that these events are too weak (i.e., too noisy) to locate individually. However, stacking individual events increases the signal-to-noise ratio of the waveforms, implying that these periodic sources are effectively stationary during the recording period.

Citation: Mikesell, T. D., K. van Wijk, M. M. Haney, J. H. Bradford, H. P. Marshall, and J. T. Harper (2012), Monitoring glacier surface seismicity in time and space using Rayleigh waves, *J. Geophys. Res.*, *117*, F02020, doi:10.1029/2011JF002259.

1. Introduction

[2]   Glaciers, rather than ice sheets, play a crucial role in fresh water storage, and marine-terminating glaciers have been shown to be major contributors to global sea level rise [*Meier et al.*, 2007]. Furthermore, marine-terminating glaciers respond quickly to changes in climate [*Truffer and Fahnestock*, 2007], while glacier flow rates [*Howat et al.*, 2007] and iceberg calving [*Jacobs et al.*, 1992; *Rignot and Kanagaratnam*, 2006] affect the glacier mass balance. Characterizing these glacier phenomena is crucial to understanding and predicting future change to glacial systems. Monitoring seismicity associated with ice movement, fracturing, and crevassing is one method to characterize glacier changes remotely. For example, *Ekstrom et al.* [2006] found seasonal variations in seismic activity in Greenland's outlet glaciers, while *Qamar* [1988] observed distinct seismic signals associated with iceberg calving at Columbia Glacier, Alaska. Building upon the latter, *O'Neel et al.* [2007] were able to discriminate between calving and other processes that generate seismic energy at Columbia Glacier based on the unique frequency spectra of iceberg calving.

[3]   Seismicity related to ice failure and glacier motion away from the terminus have also been observed by several authors. *Neave and Savage* [1970] first studied seismicity related to surface fracturing at Athabasca Glacier, while *Anandakrishnan and Alley* [1994], *Anandakrishnan et al.* [1998], and *Wiens et al.* [2008] investigated seismicity related to stick-slip motion at the bed of Antarctic ice streams. Recently, passive seismic networks have been deployed on several alpine glaciers [e.g., *Deichmann et al.*, 2000; *Stuart et al.*, 2005; *Walter et al.*, 2009] to correlate observed seismic signals with glacier dynamic events (e.g., a draining glacier lake as in *Walter et al.* [2008] and *Roux et al.* [2010]). In all of these studies, accurate event detection and location were essential to correlate observed seismic signals with glacial and subglacial processes. Furthermore, in each of these recent alpine glacier studies except *Roux et al.* [2010], body (i.e., compression and shear) waves were used to locate the seismic source region.

[1]Géoazur, Centre National de la Recherche Scientifique (UMR 6526), Observatoire de la Côte d'Azur, Université de Nice Sophia-Antipolis, Valbonne, France.

[2]Formerly at Center for Geophysical Investigation of the Shallow Subsurface, Department of Geosciences, Boise State University, Boise, Idaho, USA.

[3]Center for Geophysical Investigation of the Shallow Subsurface, Department of Geosciences, Boise State University, Boise, Idaho, USA.

[4]Alaska Volcano Observatory, U.S. Geological Survey, Anchorage, Alaska, USA.

[5]Department of Geosciences, University of Montana, Missoula, Montana, USA.

Corresponding author: T. D. Mikesell, Center for Geophysical Investigation of the Shallow Subsurface, Department of Geosciences, Boise State University, 1910 University Dr., Boise, ID 83725, USA. (dmikesell@cgiss.boisestate.edu)
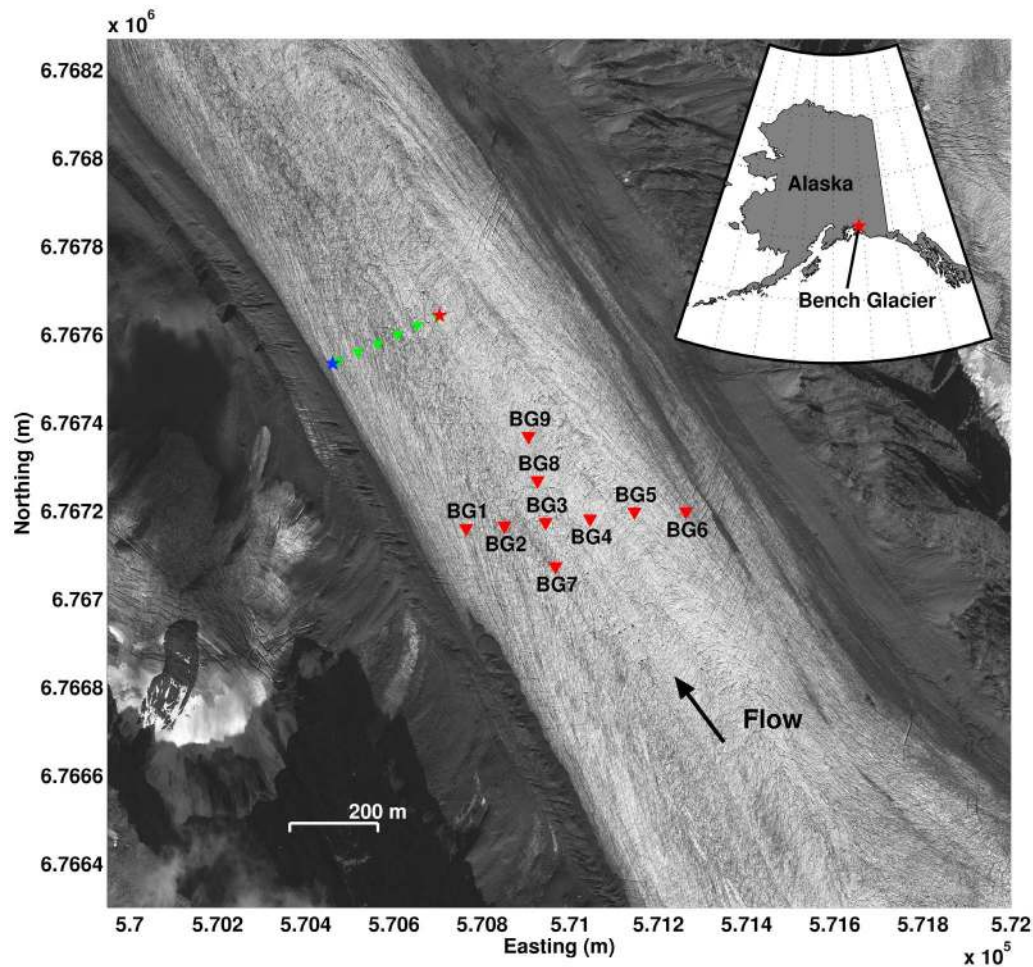
Figure 1. Bench Glacier active (green triangle) and passive (red triangle) seismic sensors. The active P wave (red star) and S wave (blue star) sources are indicated. We overlay the locations on a 0.5 m resolution World View 1 satellite image from early September 2009. Inset: Location of Bench Glacier, Alaska, USA.

[4] We present an analysis of Rayleigh wave seismicity recorded with a passive seismic array at Bench Glacier (Figure 1). This valley glacier in south-central Alaska's Chugach Mountains is approximately 7 km long, 1 km wide and ∼180 m thick beneath the array [*Anderson et al.*, 2004; *Bradford et al.*, 2009]. The array is approximately 3000 m up-glacier from the terminus and 1500 m down-glacier from an icefall. The nine-station array lies below the equilibrium line altitude in a thicker section of the glacier where the stress state is, on average, compressive or compressive along centerline due to the shallow bed slope relative to the up-glacier slope [e.g., *Bradford et al.*, 2009, Figure 5]. The seismometers are spaced ∼100 m apart in a cross pattern (Figure 1). There is little topography in this section of the glacier [e.g., *Bradford et al.*, 2009, Figure 3] and the maximum difference in elevation between seismometers is ∼25 m.

[5] From 9 August to 15 August 2007, up to nine synchronized 3-component Mark Products L28 seismometers continuously recorded ice-surface particle velocity at Bench Glacier at a sample rate of 250 samples per second on RefTek-130 digitizers. The three metal spikes on each sensor were removed; the sensors were then buried 10 cm below the ice surface, covered and packed with broken ice and rocks, and if needed, reset after melt-out (on average every two days). Similar to *Walter et al.* [2008], we apply a zero-phase band-pass filter with corner frequencies 10–80 Hz to all of the continuous data. We then spline interpolate the data by a factor of 10 and remove the L28 instrument response over this band (M. Haney et al., Causal instrument corrections for short-period and broadband seismometers, submitted to *Seismological Research Letters*, 2011).

[6] From here we begin our analysis of the Bench Glacier surface seismicity. Using cross-correlation with a Rayleigh wave reference waveform, we detect thousands of surface seismic events related to brittle ice failure. We categorize the events into 3 types. Type A events are dominated by a Rayleigh wave, but have a noticeable P wave on the vertical component. Type B and C events lack a noticeable P wave, and have a higher background noise level compared to type A events. We locate the seismic source region in time and space using the Rayleigh wave arrival-time information. *Roux et al.* [2010] take a similar approach to locate seismicity related to crevassing, which they link to a nearby draining glacier lake. However, in their approach they use

the STA/LTA method [*Earle and Shearer*, 1994] to identify icequakes.

[7] In section 2 we describe the techniques used in our analysis. We develop a reference waveform containing a large Rayleigh wave. Cross-correlating this reference waveform with the continuous data, we identify sections of data having a similar Rayleigh wave. Following the strategy outlined by *Roux et al.* [2010], we calibrate our ice velocity model from active seismic data acquired near the passive array (Appendix A) and locate event epicenters in time and space using arrival times derived from cross-correlation lag times. We also develop a Rayleigh wave magnitude scale that we can relate to the seismic moment.

[8] Our results are divided into two parts. In section 3.2 we focus on type A events related to a single crevasse which propagates in two directions away from the nucleation point. We go on to estimate the propagation rate, and we use the Rayleigh wave amplitudes to estimate a bulk ice attenuation (Q), as well as the seismic moment of individual type A events. Assuming an extensional ice failure model related to crevasse formation, we use the seismic moment to estimate the volumetric change during failure. In section 3.3, we focus on type B and C events, for which we observe a diurnal periodicity. In section 4.2 we discuss the relationship between the observed seismicity and diurnal fluctuations in temperature, surface melt, and changing water-pressure at the glacier bed.

2. Methods

2.1. Creating a Reference Waveform

[9] Cross-correlation methods enable us to detect seismic events having high signal coherency with a reference waveform [*Schaff and Beroza*, 2004]. For example, if the reference waveform is dominated by a Rayleigh wave, then sections of continuous data with similar Rayleigh waves will have a large correlation coefficient (CC). The CC value ranges from 0 to 1, with 1 being perfect coherency over the given time window and 0 being no coherency [*Schaff and Richards*, 2004]. Setting a threshold value for the CC, we can – in an automated way – identify time sections of continuous data that look very similar to the reference waveform. Based on studies in earthquake seismology [e.g., *Schaff and Richards*, 2004, 2011], we propose that this approach improves our ability to detect low amplitude near-surface events having similar source mechanisms.

[10] In the example presented here, we look for time periods dominated by impulsive Rayleigh waves in order to find events related to shallow ice failure. We search for Rayleigh waves because *Walter et al.* [2009] estimate that 99% of the seismic events they identify at Gornergletscher, Switzerland, are shallow events from crevasses that extend no deeper than ∼20 m below the surface. *Walter et al.* [2008] show that deeper events (i.e., below this crevasse cutoff depth) show no obvious Rayleigh wave. Furthermore, multiple authors have shown that for shallow ice failure, a strong Rayleigh wave is preceded by lower amplitude P and S waves [e.g., *Neave and Savage*, 1970; *Deichmann et al.*, 2000; *Stuart et al.*, 2005; *Walter et al.*, 2009].

[11] To create our reference waveform, we manually select an event that is recorded on the vertical component across the entire seismic array. We determine the existence of a

dominant Rayleigh wave by analyzing the instantaneous polarization [*Vidale*, 1986], whereby we observe the retrograde elliptical polarization between the vertical and horizontal components common to Rayleigh waves [e.g., *Stein and Wysession*, 2003, p. 89]. To improve the reference waveform signal-to-noise ratio (SNR), we align the Rayleigh waves on the maximum correlation lag between one station and the all of the others and stack. We then center the stacked waveform within a time window and taper the first and last 5% of the window to zero. Constructing a reference waveform in this way amplifies the already dominant Rayleigh wave, while suppressing the P wave and background noise.

2.2. Event Location

[12] For a homogeneous ice model with velocity V, the arrival time of the Rayleigh wave (d_i) at station i, located at (x_i, y_i) is

$$d_i = t + \left(\sqrt{(x_i - x)^2 + (y_i - y)^2} \right)/V, \qquad (1)$$

from a source located at the surface with model parameters $\mathbf{m} = (t, x, y)$, where t is the event origin time and (x, y) is the event epicenter. After a truncated Taylor expansion around a starting guess $\mathbf{m}_0$, we arrive at the linearized set of equations [*Geiger*, 1910]:

$$G\Delta\mathbf{m} = \Delta\mathbf{d}, \qquad (2)$$

where $\Delta\mathbf{m}$ is a 3-dimensional vector of model parameter updates, $\Delta\mathbf{d}$ is the n-dimensional data vector of the difference between observed and calculated travel times, and G is the $n \times 3$ matrix of partial derivatives of the data with respect to the model parameters:

$$G = \begin{bmatrix} \dfrac{\partial d_1}{\partial t} & \dfrac{\partial d_1}{\partial x} & \dfrac{\partial d_1}{\partial y} \\ \cdot & \cdot & \cdot \\ \dfrac{\partial d_n}{\partial t} & \cdot & \cdot \end{bmatrix}. \qquad (3)$$

This epicenter inversion procedure is similar to other recent studies of glacier seismicity [e.g., *Roux et al.*, 2010; *Walter et al.*, 2011].

[13] In Appendix A we estimate the Rayleigh wave velocity in ice to be $V = 1668$ m/s from active seismic experiments. Taking our starting model $\mathbf{m}_0 = (0, 0, 0)$ (i.e., the center of the array and relative origin time equal to zero) and the relative Rayleigh wave arrival times as data, we invert equation (2) to estimate the epicenter and relative origin time of an icequake. We iteratively update the model by $\Delta\mathbf{m} = G^\dagger \Delta\mathbf{d}$ until the model fits the data on average within one standard deviation σ_d. If the solution does not converge within 10 iterations the event is removed from the data set. Here $G^\dagger = (G^T G)^{-1} G^T$, which is the ordinary least squares inverse of G [*Aster et al.*, 2005]. We estimate the model parameter standard deviations as $\sigma_{m_i} = \sqrt{\sigma_d diag((G^T G)^{-1})_i}$, where $(G^T G)^{-1}$ is assumed diagonal.

2.3. Attenuation

[14] In addition to the icequake epicenters, the amplitudes of the Rayleigh waves offer insight into the glacier ice
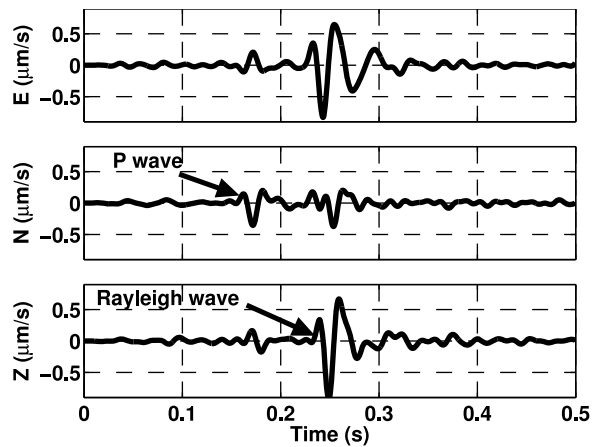
Figure 2. Three-component wavefield for a surface-fracture event at station BG1. The dominant phase at $t \sim 0.25$ s is the Rayleigh wave and the phase at $t \sim 0.15$ s is the direct P wave. The data are spline interpolated by a factor of 10 and the instrument response deconvolution is performed over the frequency range 10–80 Hz. Amplitudes for the three components are as follows: Z, positive is downward; E, positive is eastward; N, positive is northward.

properties and the size of the brittle failure. For a homogeneous elastic medium with attenuation, the amplitude A at a given station i at distance R_i from a point force source is [e.g., *Lin et al.*, 2011]:

$$A(R_i) = A_0 \frac{1}{\sqrt{R_i}} e^{-\alpha R_i}, \qquad (4)$$

where $1/\sqrt{R_i}$ is the Rayleigh wave geometric spreading factor, A_0 is the source force amplitude at the icequake epicenter, and α is the attenuation decay constant related to the seismic quality factor: $Q = f_0/(\alpha V_0)$. V_0 is the Rayleigh wave phase velocity at frequency f_0 [e.g., *Aki and Richards*, 2002, chapter 7.1]. If the ice were non-attenuative ($\alpha = 0$), the geometrically corrected Rayleigh wave amplitudes should be constant for any R. Residual amplitude decay with distance R can be attributed to energy loss by seismic scattering and intrinsic attenuation. We estimate α by fitting a linear function to the natural log of the geometrically corrected amplitudes using bi-square weighted least squares. From this we can calculate a bulk Q for the glacier ice.

2.4. Seismic Moment

[15] We also estimate the co-seismic slip using event amplitudes. The seismic moment is directly related to the amount of slip and/or opening along a crevasse. Toward this goal, we derive an icequake magnitude M_S using the following relationship

$$M_S = \log_{10}(A/T) + F(R), \qquad (5)$$

where A is the maximum ground displacement in microns of the Rayleigh wave with period T, and F is a spreading correction factor based on epicentral distance R. This relationship is derived from more general magnitude relationships [e.g., *Lay and Wallace*, 1995, equation 9.30], where we set the source

and station correction terms equal to zero and the geometric spreading term F only depends on epicentral distance.

[16] From the best fit line in section 2.3, we take the amplitude A at $R = 0$ (i.e., the y-intercept) as a measure of the initial force amplitude (A_0) at the icequake epicenter. We assume that this value is corrected for geometric spreading and attenuation. Hence, we can simplify our magnitude estimate to $M_S = \log_{10}(A_0)$. Furthermore, we relate our magnitude estimate M_S to the seismic moment M_0 with an empirical relation (in dyne-cm) commonly used for earthquakes [*Lay and Wallace*, 1995, equation 9.44]:

$$\log_{10}(M_0) \approx 1.5 M_S + 16.1. \qquad (6)$$

This allows us to make inferences about the amount of slip or opening along a fracture for a given failure mechanism.

3. Results

3.1. Reference Waveform and Event Detection

[17] We select an event with a large Rayleigh wave on 10 August 2007 when seven stations were recording. The three components of the wavefield at station BG1 are shown in Figure 2. The dominant phase on the Z component at $t \sim 0.25$ s is the Rayleigh wave. The smaller amplitude phase at $t \sim 0.15$ s is the direct P wave. This event looks very similar to previously studied 3-component waveforms from shallow ice failure [e.g., *Walter et al.*, 2009, Figures 2a and 2b].

[18] To compare the similarity of the event across the entire array, we compare the amplitude-normalized vertical-component wavefield at stations BG1 through BG7 (Figure 3a). We observe both P and Rayleigh waves, and looking at the signal before the Rayleigh wave, it is apparent that the noise level increases with epicentral distance. The differential moveout of the P and Rayleigh waves, due to differences in the propagation velocity, is also apparent. We do not show stations BG8 and BG9 because recording at these stations began approximately one hour after this event occurred. We create the reference waveform by aligning the Rayleigh waves at each station and stacking (Figure 3b).

[19] We cross-correlate the continuous data on station BG3 with the reference waveform from 10 August 2007 02:00 GMT to 12 August 2007 00:00 GMT. We choose BG3 because it is the only station that was not reset due to melt-out. It is also the center station of the array. We identify 8734 events having a correlation coefficient CC ≥ 0.5 with the reference waveform. This CC value was chosen after visual inspection of waveform plots such as that in Figure 4, which shows the 8734 events. The first and last 5% of the waveforms in the 0.5 s window are tapered to zero. (For CC values below 0.5 we began to identity noise rather than signal. This was apparent because of the fact that we no longer had a coherent arrival in the vertical direction.) The events in Figure 4 are aligned on their maximum correlation with the reference waveform, and each event is normalized to unit amplitude. We identify three different types of events (A, B, and C) based on the Rayleigh wave characteristics. We draw a black box around each group of events in Figure 4, and we identify the event type in the upper right corner of each box. The dashed line represents 11 August 2007 00:00 GMT.
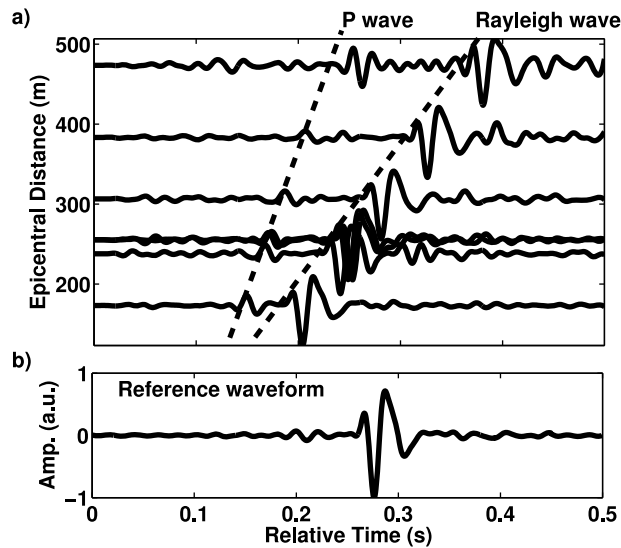
Figure 3. (a) Amplitude normalized vertical-component waveforms at stations BG1 through BG7 for the event shown in Figure 2. The waveforms are plotted as a function of epicentral distance; however, $t = 0$ does not correspond to the origin time. (b) The reference waveform is generated by aligning all waveforms in Figure 3a on the Rayleigh wave and summing. This suppresses the P wave and background noise.

[20] Type A events have an identifiable P wave arrival at $t \sim 0.2$ s and are dominated by an impulsive Rayleigh wave. The event shown in Figure 3a is a characteristic type A event. Type B events have a Rayleigh wave that changes with time and lack an obvious P wave (shown in section 3.3). Type C events also lack a P wave, but the Rayleigh wave is constant through time. Furthermore, we observe that type B and C events occur twice over the 46 hours with type C events preceding type B events. Because we identified these events using the Rayleigh wave reference waveform, we assume that the source is located near the glacier surface. In the following sections we analyze type A events separate from type B and C events due to their different SNR characteristics and our ability to accurately locate individual event epicenters.

3.2. Type A Events

3.2.1. Epicenter Locations

[21] In order to determine the relative Rayleigh wave arrival-times for a given type A event, we cross-correlate the 0.5 s waveforms at each station with the waveform at a reference station. This reference station is different than the reference station used in the event search method. This new reference station can change for each event, and is determined as the station which the Rayleigh wave arrives first. In this way, we generate differential arrival-time data relative to the reference station for each type A event. Using the $10\times$ interpolated waveforms allows subsample (≤ 4 ms) estimates of Rayleigh wave arrival-time differences. Previous authors have shown that differential arrival-time estimates by cross-correlation reduce error estimates in the model parameters by orders of magnitude [*Schaff and Beroza*, 2004; *Schaff and Richards*, 2011]. Even though we have

interpolated waveforms, we estimate $\sigma_d = 4$ ms (i.e., the original sample interval) which leads to errors in epicenter locations on the order of 5 to 10 m. Similar errors were estimated by *Neave and Savage* [1970] and *Roux et al.* [2010].

[22] We estimate the epicenter location for type A events, requiring that each event has a SNR ≥ 4 at 5 or more stations. We compute SNR as the maximum Rayleigh wave amplitude divided by the root-mean square value of the entire 0.5 s window. This is not the common SNR estimate. However, we extract many small windows ($\sim$8000 events at 9 stations) around the Rayleigh wave, and it is difficult, in an automated way, to estimate the noise in the 0.5 s window while ensuring that we do not sample the Rayleigh or P waves. Moreover, as long as we are consistent, the SNR estimation method should have no effect on the final number of located epicenters. We locate 654 type A events. The lengths of the bars in Figure 5 represent the 2σ error for the estimated model parameters in Easting and Northing directions. We determine absolute time after the inversion by adding the relative origin time estimate to the arrival time of Rayleigh wave at the reference station. The chronological color scheme of the event epicenters in Figure 5 shows that isolated event clusters occur at different times on the glacier surface.

[23] *Neave and Savage* [1970] first observed linear event clusters parallel to existing crevasses which struck 55° to glacier flow. The event epicenters that we locate occur preferentially near the glacier edges. The solid black lines on the left edge of the glacier indicate minimum and maximum directions of shear stress (σ_s) due to pure shear between the flowing glacier and the stationary valley walls. The light blue line indicates the maximum compressive stress direction, approximately 45° to the valley wall in the up-glacier direction. We note that in the satellite image we observe marginal crevasses on both sides of the glacier that open
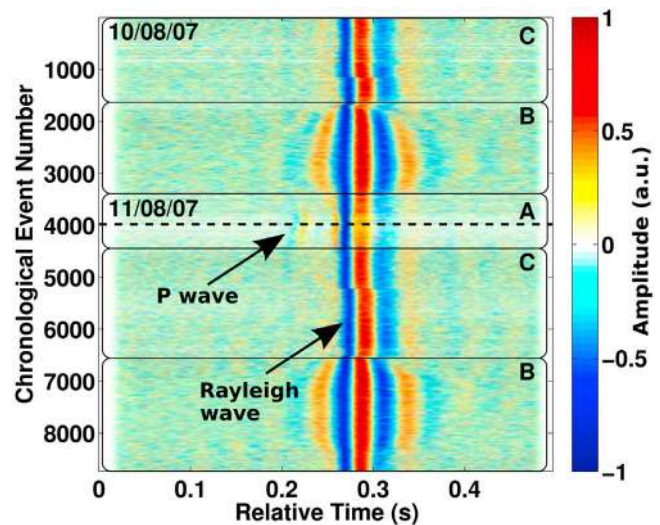

Figure 4. Amplitude normalized events identified from 10 August 2007 02:00 GMT to 12 August 2007 00:00 GMT at BG3 using the cross-correlation search technique and reference waveform in Figure 3b. The correlation coefficient threshold is CC ≥ 0.5. Events are divided in three types: A, B and C. See text for description of different event types.
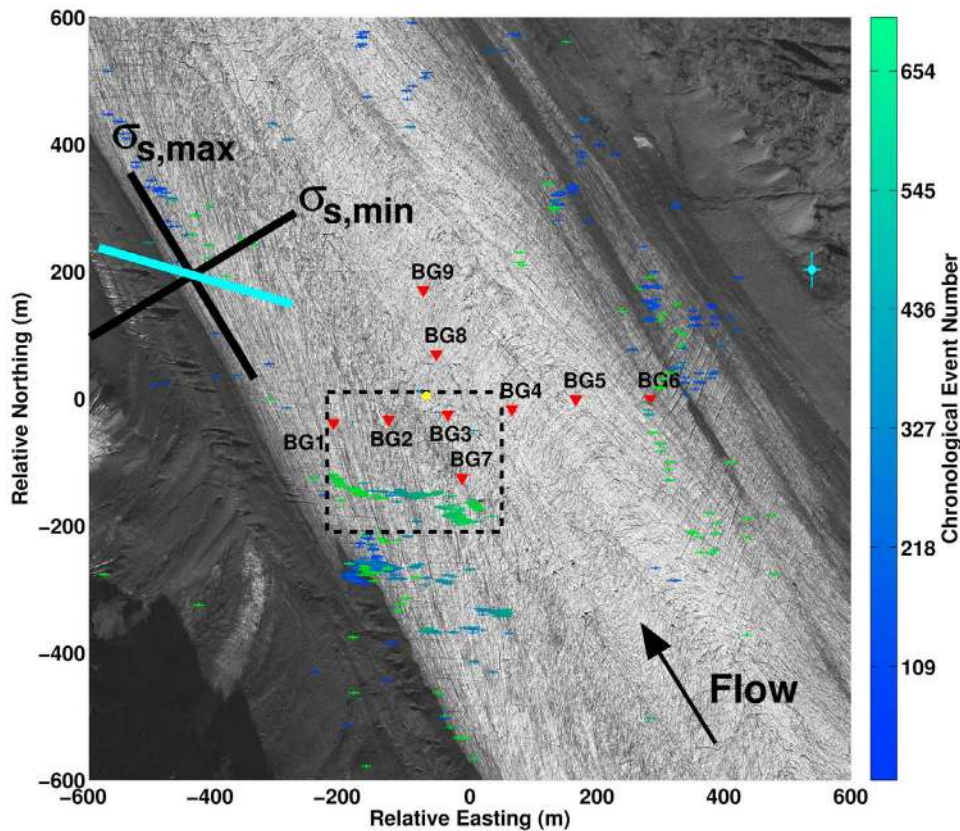
Figure 5. Icequake epicenter locations for 654 events meeting the SNR criteria in section 3.2.1 and converging to a solution that fits the data, on average, to within one standard deviation. The solid black lines on the left edge of the glacier indicate the inferred minimum and maximum shear stress (σ_s) directions. Cyan line indicates the maximum compressive stress direction. Yellow and cyan dots indicate locations of type B and C events, respectively.

perpendicular to the maximum compression direction. As expected, the crevasse pattern rotates as we move toward the center of the glacier, with crevasses opening perpendicular to the glacier flow direction. Crevasse pattern observations similar to these have been made on other alpine glaciers [e.g., *Harper et al.*, 1998] and are consistent with general crevasse patterns expected in valley glaciers experiencing shear from the valley walls [*Cuffey and Paterson*, 2010].

[24] In addition to events occurring near the valley walls, we see a subset of our event locations (235 events) forming a nearly linear feature that we highlight in the dashed box and show in a zoomed view in Figure 6. The chronological color scale is reset so that the first event is blue and the last is green in Figure 6. These events align in a parallel direction with the dominant fracture pattern (dashed cyan line) in the satellite image, with extensional opening likely happening normal to this direction. Interestingly, the seismic events start in the center of the event cluster and propagate away in both directions, with the left end curving to the North and the right curving to the South (possibly splaying into two features). *Neave and Savage* [1970] observed three different patterns of crevasse opening: (1) events start near the glacier margin and migrate toward the center of the glacier; (2) events start near the center and migrate toward the edge of the glacier; (3) events begin in the middle and migrate away from the initial fracture point. We see the

third pattern in our data, with epicenters starting in a central position and moving away from the nucleation point in both directions.

3.2.2. Attenuation and Seismic Moment

[25] We automatically pick the maximum amplitude of the Rayleigh wave at each station for the subset of 235 type A events in Figure 6. With $V_0 = 1668$ m/s and $f_0 = 45$ Hz, the dominant frequency of the event and center of the band-pass, we estimate a mean $\bar{Q} = 42 \pm 28$. To illustrate our Q estimation process we show the amplitude picks for a single event in Figure 7. The y-axis is the natural log of the geometrically corrected amplitude. We linearly fit the points and estimate $Q \approx 35$. Amplitude deviations from the best fit line are attributed to lateral heterogeneity in the glacier, as well as coupling variations between the stations and the ice surface. The estimated mean $\bar{Q}$ value falls within previously published ice attenuation estimates from active seismic experiments (e.g., Q = 22 to 220 in *Smith* [2007]). Finally, we note that only 218 events contribute to the $\bar{Q}$ estimate because for some events we obtain non-physical values (i.e., negative Q values or Q > 300). In those cases, we discard the Q estimate, assuming that we have incorrect R estimates due to incorrect icequake locations or imprecise automated amplitude picks.

[26] From the 218 events used in the $\bar{Q}$ estimate, we estimate the mean surface wave magnitude $\bar{M}_S = -0.76 \pm 0.35$.
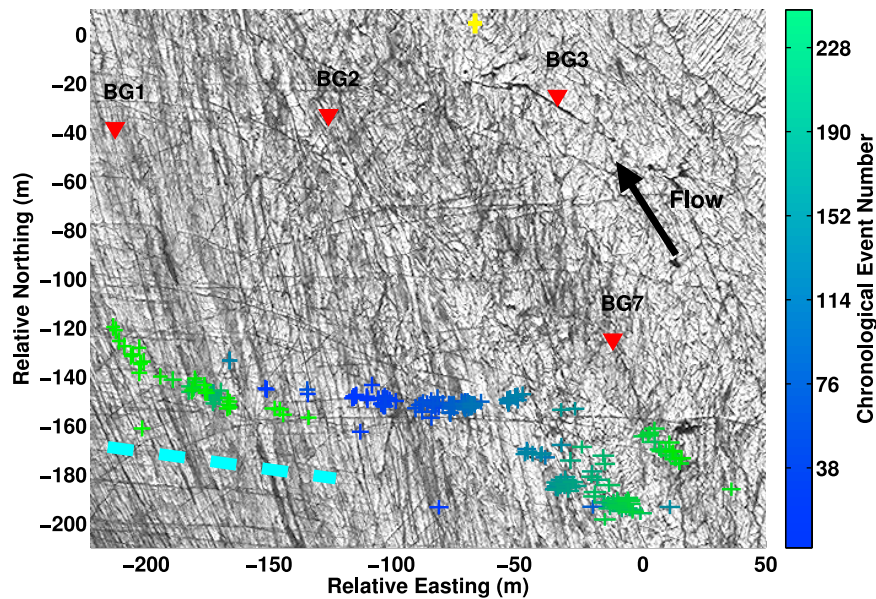
Figure 6. Zoom around the epicenters in the southwest corner of the seismic array identified by the dashed box in Figure 5. The 235 type A events start in the middle and propagate to each end of the fracture over 200 minutes. The dashed cyan line indicates the dominant crevasse alignment relative to the valley wall.

Furthermore, we calculate the mean seismic moment $\bar{M}_0 \sim 2.33 \times 10^8$ Nm (equation (6)). These values are within an order of magnitude of the estimates of surface ice failure events found at Gornergletscher, Switzerland, based on a full-waveform moment tensor inversion [*Walter et al.*, 2009]. Furthermore, we can estimate the amount of opening along the crevasse if we take the first Lamè constant λ and shear modulus μ from Appendix A. For tensile opening, we use the relationship $\Delta V = M_0/(\lambda + 2\mu/3)$ to estimate the volume change ΔV [*Müller*, 2001] and find the mean $\bar{\Delta V}$ of these events equal to 3.1×10^{-2} m^3, also similar in magnitude to the tensile opening observed by *Walter et al.* [2009].

3.3. Type B and C Events

[27] We now turn our attention to event types B and C. In Figure 8 (left) we show a type B example (event 2001 in Figure 4). Event types B and C are more noisy than event type A. The Rayleigh wave amplitudes in Figure 2 are comparable to those in Figure 8, but the background noise level during the type B events is significantly higher. Even though the cross-correlation detection method has identified these noisier events, they did not pass the SNR criteria in the epicenter location process described in section 3.2.1. However, we can stack groups of type B and C events to increase the SNR of the Rayleigh wave, so that locating the stack becomes possible.

[28] Figure 8 (right) shows the average waveforms after stacking type B events 2000 to 2100 from Figure 4. The Rayleigh wave is now evident, indicating that constructive stacking occurred at all four stations and leading us to the conclusion that the source is relatively stationary during these 101 events. We can now locate the epicenter using the arrival-time differences from the stacked Rayleigh waves. The yellow dots in Figures 5 and 6 indicate the location after stacking type B events 2000 to 2100. A similar analysis can

be made and epicenter located (cyan dot in Figure 5) for type C events 1200 to 1300.

[29] The model parameter errors are larger for the type C stack compared to location errors less than 10 m for type A events and the type B stack. This larger error makes sense as the event occurs on the Eastern edge of the glacier, farther from the array. Furthermore, the fact that the type C location plots in the moraine, indicates that our assumption of a homogeneous ice velocity model is likely no longer valid.

3.3.1. Temporal Relationship Between Type B and C Events

[30] Because of the periodic nature of type B and C events in Figure 4, we further investigate their temporal relationship.
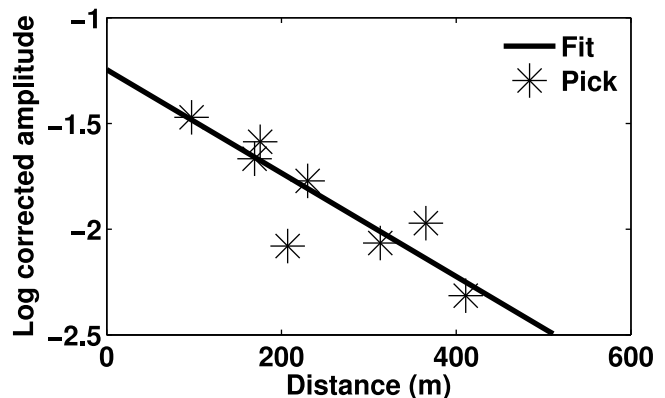

Figure 7. The natural logarithm of the geometrically corrected maximum Rayleigh wave amplitude pick as a function of epicentral distance for a single type A event. The remaining decay in the corrected amplitudes is attributed to the seismic quality factor Q. In this example we estimate $Q \approx 35$.
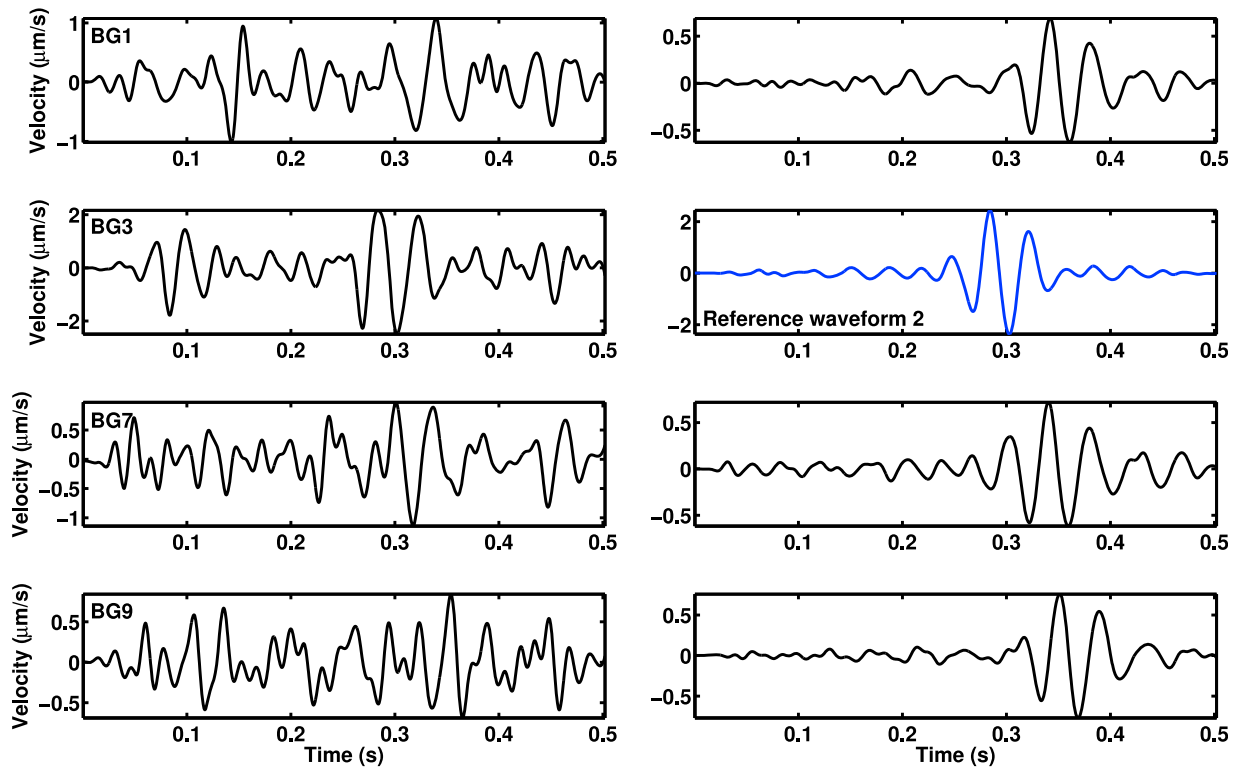
Figure 8. (left) Event 2001 at stations BG1, BG3, BG7 and BG9. (right) Stack of events 2000 to 2100 at stations BG1, BG3, BG7 and BG9. The Rayleigh wave constructively stacks over the 101 events. The blue waveform indicates the type B reference waveform.

In order to identify only type B and C events (i.e., suppress type A events), we create a new reference waveform by summing events 2000 to 2100 at BG3 (blue waveform in Figure 8). Furthermore, to ensure we minimize type A detections, we increase the correlation coefficient threshold. After visual inspection of waveform plots similar to Figure 4, a CC ≥ 0.6 suffices to suppress type A events.

[31] We extend the search to the entire data set – 9 August to 15 August 2007 – and again we search the vertical component data at BG3. We construct an event histogram (Figure 9) in order to determine if the type B and C periodicity occurs throughout the recording period. The blue line represents the number of identified events per minutes, and the green line is the nearest daily temperature measurement, taken from weather station PAVD at the Valdez, Alaska, airport (approximately 32 km to the West). The yellow shaded areas indicate daylight hours, with the first day starting at 15:00 local time (9 August 2007 00:00 GMT).
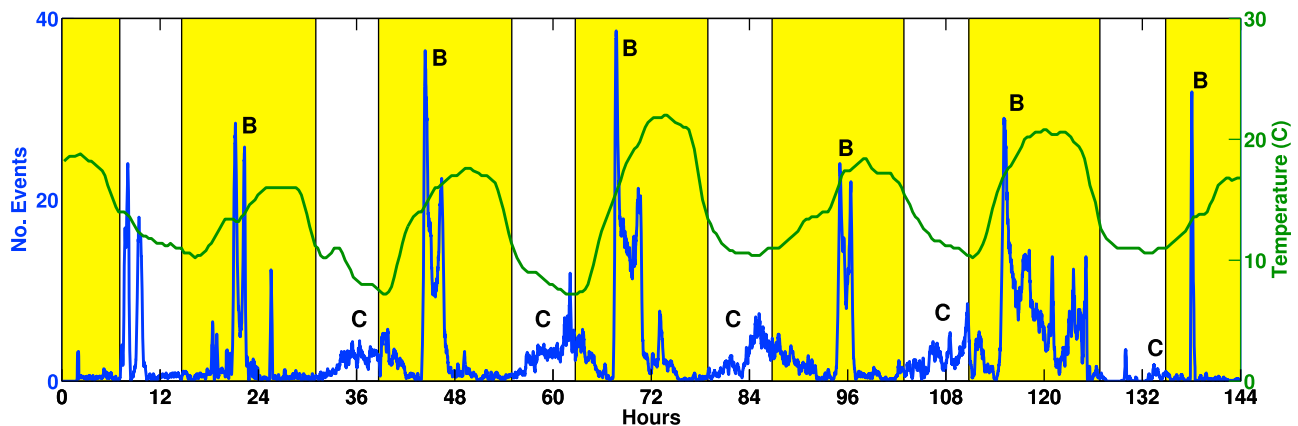

Figure 9. Events per minute (blue) identified at BG3 from 9 August 2007 00:00 GMT to 15 August 2007 00:00 GMT using the type B reference waveform (Figure 8). Time sections in yellow indicate daylight hours and the green line is temperature recorded at the Valdez, Alaska, airport 32 km away. Type B and C event clusters are indicated.
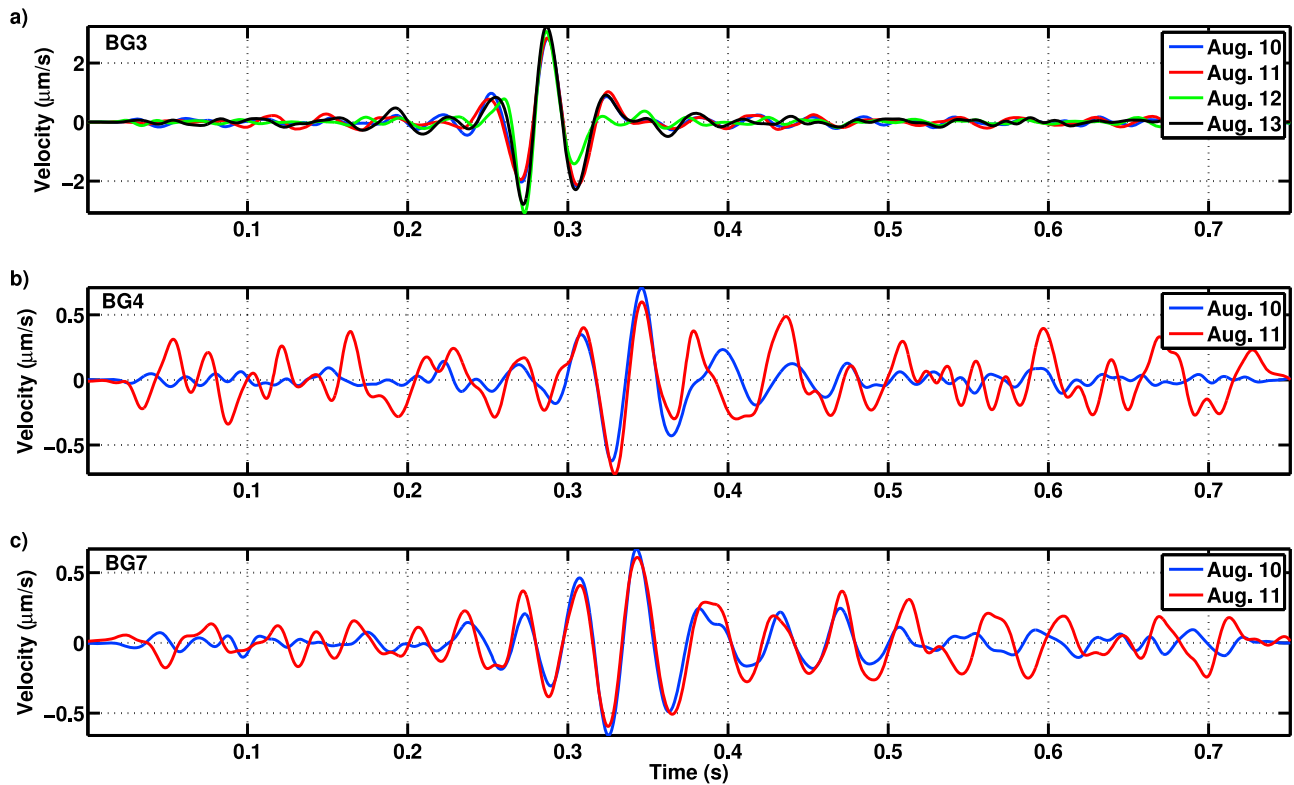
Figure 10. (a) Stacks of 101 events at the beginning of type B event onset (e.g., 10 August comes from stacking events 1900 through 2000 in Figure 4). (b and c) The same stacks of events at stations BG4 and BG7, respectively.

Type B and C event clusters are labeled on the histogram. We observe a correlation between seismic activity and temperature, with type B events preceding the daily temperature maximum in Valdez on average by 4.4 hours ± 1.2 hours. Type B seismicity has a double peak on most days. Less pronounced is the type C seismicity, which begins shortly after sunset and peaks near sunrise.

[32] Besides this relationship in time, we also want to determine the epicenter locations for type B and C events over the entire period of recording. We previously showed that type B and C events have low SNR, and we have to stack events in order determine the epicenter of a group of events. However, because the signal quality deteriorates across the array over the recording period, we are unable to determine event epicenters for groups of type B or C events as previously done. As an empirical check on the epicenters, we stack the first 101 type B events for each of the first 4 recording days to see if they stack constructively. Figure 10 shows the stack from each day in a different color. Station BG3 was the only station that was not reset during the entire recording period. We observe almost identical waveforms after stacking 101 type B events on each day. The two stations BG4 and BG7 also had fairly good coupling and did not need to be reset from 10 August to 12 August 2007. The stacks are almost identical at all stations, with the earlier days having higher SNR, likely due to better sensor-ice coupling. This leads us to infer that not only do type B events occur periodically with time, they also originate from the same region of the glacier each day relative to

our seismic array. A similar observation is made if we stack type C events.

4. Discussion

[33] Type A events are dominated by a Rayleigh wave and have higher SNR compared to the Rayleigh wave in type B and C events. A subset of type A events corresponds to the group making up the linear feature in the dashed box in Figure 5. In this example, we see that the crevasse opens from the center outward in both directions. On the western extent we see the epicenter pattern break into two separate groups. We note that it is possible that these seismic events come from two separate crevasses. It is also possible that the crevasse is deepening, which would mean our epicenter location error increases because the seismic source is not actually at the surface.

[34] For these large SNR events, the P and S wave arrivals could be picked manually and used in an inversion algorithm that combines all three wave types [e.g., *Lay and Wallace*, 1995]. This would likely improve the accuracy of icequake locations and make hypocentral location possible. Double difference methods could also be utilized to further constrain locations into linear clusters [*Waldhauser and Ellsworth*, 2000], giving more detailed insights into how the crevasse opens with time. However, automated picking of these phases can be difficult because body wave amplitudes suffer from 3D geometric spreading as compared to 2D geometric spreading for Rayleigh waves [e.g., *Stein and Wysession*, 2003, p. 187]. This is evident in our data when comparing
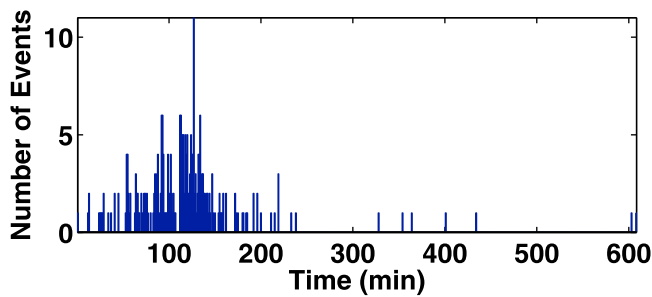
Figure 11. Number of events per minute for the 235 events making up the crevasse in Figure 6. The majority of events (226) occur within the first 200 min.

the P- and Rayleigh wave amplitudes as distance increases in Figure 3a. Furthermore, this illustrates why we emphasize the use of Rayleigh waves in our work.

[35] Attenuation estimates as a function of space and time in glaciers may provide valuable glacier properties. For example, scattering Q can be related to heterogeneity (fractures, voids, etc.) in the glacier, while intrinsic Q can be attributed to water saturation and ice temperature [e.g., *Peters et al.*, 2012]. Here, we are limited to two days of good quality data at all nine stations, and lack the complete azimuthal coverage to correct Rayleigh wave amplitudes for possible radiation pattern effects. If future arrays avoid meltout and changes in sensor-ice coupling, and if we compensate amplitudes for radiation effects using moment tensor inversion solutions, then it might be possible to use Q to estimate the dominant fracture orientation in the ice and thus infer local strain fields. Alternatively, temporal changes in Q may be related to changing water content within the glacier ice, an important parameter for many glacier studies. In the remaining discussion we look at the spatial and temporal relationships we observe in these data and try to link them to the glacier system.

4.1. Type A Events: Crevasse Opening

[36] We cannot determine if the crevasse in Figure 6 is pre-existing or new based on the seismic data, but based on observations by *Neave and Savage* [1970], it is likely that this is a new crevasse. The 235 events defining this crevasse occur over approximately 10 hours, but 226 events occur within the first 200 minutes. We plot a histogram of the events in Figure 11. The total extent of the crevasse is 253 m, taken from the epicenters with the farthest separation in Figure 6. We estimate that the fracture propagates in one direction at an average rate of 126.5 m/200 min = 0.63 m/min. This is considerably slower than observations by *Neave and Savage* [1970]. Their observations come from crevasses of similar length; however, the maximum number of epicenters they use is 23. Therefore, it is possible that they missed a considerable number of low amplitude seismic events that we detect with the cross-correlation search technique. They use a different method to pick arrival times which could lead to differences in the accuracy of epicenter locations and thus different estimates of crevasse propagation rates.

[37] Our field observations at Bench Glacier indicate that crevasses can be on the order of hundreds of meters long, up to tens of meters deep, and centimeters to meters wide. Small

values of volumetric change from the seismic moment, combined with the field observations of long crevasses seem to suggest that crevassing involves long periods of small-magnitude co-seismic ice failure. The detection of thousands of events in the short period of recordings in this study corroborate this model.

4.2. Type B and C Events: Seismicity Related to Diurnal Glacier Cycles

[38] The lag time between type B events and the daily maximum temperature appears semi-constant during the days we record seismicity at Bench Glacier. Using the five days during the middle of recording, where the lag trend seems to be stable, the maximum daily temperature lags the type B seismicity peak by 4.4 hours ± 1.2 hours. On the first day, it looks as if the type B peak is delayed compared to later trends. We note that the weather station data indicate a low pressure system on that day, with the barometric pressure increasing and stabilizing for the remainder of the recording period starting on day two. Therefore, it is possible that atmospheric pressure (or more likely precipitation conditions) had an influence on the glacier motion and resulting seismicity on that first day. With time, the seismic data quality diminishes due to melt-out and decreased sensor-ice coupling. This possibly explains the lack of identifiable C events near hour 132 and the lack of multiple B peaks following that.

[39] If the type B and C seismicity respond to changes in precipitation, it is likely that water pressure at the bed, which changes due to surface water input, is responsible rather than surface temperature directly. *Neave and Savage* [1970] did not see a relationship between crevasse formation and surface temperature. Furthermore, diurnal pressure fluctuations at the glacier bed have been observed during this time of year. *Fudge et al.* [2008] show diurnal bed pressure fluctuations at Bench Glacier in 2002, 2003, and 2004 during the month of August related to changing water levels on the order of 10 to 30 meters within the glacier system. Along those lines, *Walter et al.* [2008] correlate observed deep seismic events with subglacial water pressure changes on Gornergletscher, Switzerland. Perhaps bed pressure oscillations affect the surface seismicity at Bench Glacier. *Roux et al.* [2010] observed increased surface seismicity during glacial lake drainage. It could be that the surface seismicity is caused by an increase in strain rate in the glacier surface when the glacier flows fastest. However, for the data set shown here, we lack GPS surface motion and bed pressure observations to develop any sort of temporal relationship between these quantities. From this we conclude that it may be possible that surface seismicity could be used to monitor glacier motion cycles if sensor-ice coupling could be improved over long time periods.

[40] Finally, we propose possible explanations as to what causes the observed type B and C seismicity, if it is indeed related to subglacial water pressure. One possibility is related to subglacial water pressure. As pressure increases, U-shaped valley glaciers lift and fall outward toward the sides of the valley. This could result in surface fracturing. Another possibility is that bed topography plays a role. As subglacial water pressure increases and the bed floods, glaciers often accelerate downstream [e.g., *Harper et al.*, 2007]. Given variations in the bed topography, the glacier may move over a point in the bed
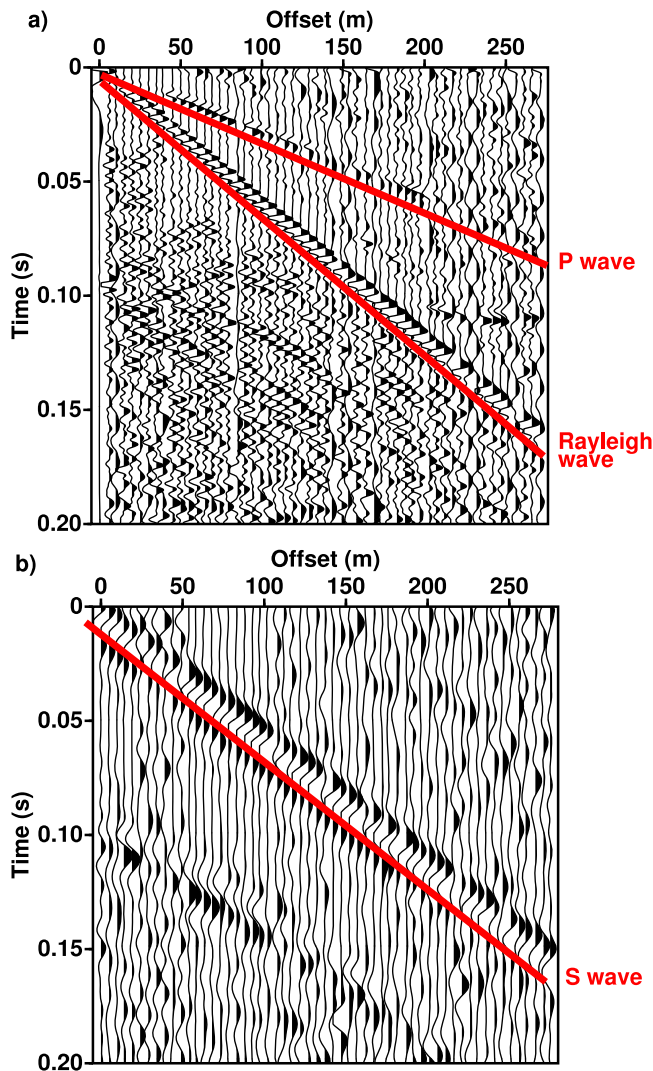
a)

b)

Figure A1. (a) Trace normalized active seismic slide hammer data with 20–200 Hz zero-phase band-pass filter. P wave velocity estimate is 3636 m/s and the Rayleigh wave velocity is 1668 m/s. There is little Rayleigh wave velocity dispersion in this frequency band. (b) Active seismic horizontal shear wave (SH) data processed the same as the P wave data. The S wave velocity estimate is 1825 m/s. Shot locations are shown in Figure 1.

that causes increased strain locally and results in ice surface failure that is stationary in time. The final possibility is that the seismic energy comes from a single crevasse slowly opening, but over the course of a few days. Thus, appearing stationary over the period of our observation. We have no evidence at this point that crevasses open at the same rate, therefore, it is possible that we are observing a crevasse open slowly compared to the crevasse we observed open over 200 minutes.

5. Conclusion

[41] We use a cross-correlation search method to identify seismic sources in glacier ice that generate a Rayleigh wave. We observe thousands of near-surface icequakes in continuous passive seismic recordings from a nine station array at

Bench Glacier, Alaska, USA. Of all the events, we locate 654 events with high signal-to-noise ratios using a Rayleigh wave travel-time inversion. One cluster of epicenter locations is related to a single crevasse. Based on the surrounding crevasse patterns we observe in a satellite image and the known stress relationship between the glacier and the valley walls, we interpret this seismic cluster as an opening crevasse that propagates 253 meters in 200 min.

[42] We analyze the Rayleigh wave amplitudes in this cluster to estimate seismic attenuation in the ice, which may serve as a (time-lapse) monitoring tool in future studies. Developing a relationship between the geometrically corrected Rayleigh wave amplitudes and the seismic moment, we estimate the mean volumetric opening along the crevasse. The small amount of opening leads us to infer that many small events lead to the crevasse opening. Furthermore, a diurnal periodicity in seismicity indicates a relationship between surface strain rates and bed pressure. We hypothesize that surface seismicity is largely controlled by surface melt and subglacial water pressure changes. Finally, we show that a waveform cross-correlation method is an efficient way to identify shallow seismicity in this glacier system. This implies that in other glacier and ice sheet systems, this method can be used to identify seismicity associated with a specific failure mechanism.

Appendix A: Active Seismic Experiment

[43] During passive data collection, we acquired active P and S wave seismic data at another location on the glacier. 10 Hz vertical component P and S wave receivers were spaced 5 m apart and set into holes drilled in the ice surface (green triangles in Figure 1 show a subset of receiver positions). We use one active shot from a slide hammer to estimate the P and Rayleigh wave ice velocities. Figure A1a shows the slide hammer shot record from a source near the center of the glacier (red star in Figure 1). The shot record is band-pass filtered between 20 and 200 Hz and a root-mean square Automatic Gain Control [e.g., *Yilmaz*, 2001, p. 85] is applied with a window of 0.025 s. We trace the P and Rayleigh wave move outs (red lines) and estimate the velocities to be 3636 m/s and 1668 m/s, respectively. In this frequency band, we see little Rayleigh wave velocity-frequency dispersion [e.g., *Aki and Richards*, 2002, chapter 7.1], indicating that the velocity model can be satisfied with a homogeneous half-space.

[44] Figure A1b shows the shot record for a shear wave source along the same line (blue star in Figure 1). We used transverse component geophones and a sledge hammer hit into a railroad tie with spikes anchoring it to the ice surface. The sides of the tie were cut to 45 degrees and we hit each side four times. The polarity for one side of hits was reversed and then all shots stacked together to suppress P wave energy generated by the 45 degree hammer blow. Using the direct S wave, we estimate the horizontally polarized shear (SH) wave velocity to be 1825 m/s.

[45] Crystalline ice density is 0.917 g/cm^3 at 0°C [e.g., *Petrenko and Whitworth*, 2002, Table 2.3]. Assuming five per cent air bubbles in the near-surface glacier ice [*West et al.*, 2007; *Bradford et al.*, 2009], we estimate the glacier ice density to be 0.87 g/cm^3. With the active source velocity estimates and our density estimate, we compute the elastic

moduli of the ice. The shear modulus μ = 2.9 GPa, and the first Lamè constant λ = 5.71 GPa. This yields an apparent Poisson ratio of 0.33, a common value for isotropic polycrystalline ice [*Gammon et al.*, 1983]. The elastic moduli can be used to estimate the amount of slip during shear or volumetric change during extensional fracturing. Finally, we say apparent Poisson ratio because we do not take into account seismic velocity anisotropy due to fracture patterns.

References

Aki, K., and P. G. Richards (2002), *Quantitative Seismology: Theory and Practice*, 2nd ed., Univ. Sci. Books, Sausalito, Calif.

Anandakrishnan, S., and R. B. Alley (1994), Ice stream C, Antarctica, sticky spots detected by microearthquake monitoring, *Ann. Glaciol.*, *20*, 183–186.

Anandakrishnan, S., D. D. Blankenship, R. B. Alley, and P. L. Stoffa (1998), Influence of subglacial geology on the position of a West Antarctic ice stream from seismic observations, *Nature*, *394*(6688), 62–65, doi:10.1038/27889.

Anderson, R. S., S. P. Anderson, K. R. MacGregor, E. D. Waddington, S. O'Neel, C. A. Riihimaki, and M. G. Loso (2004), Strong feedbacks between hydrology and sliding of a small alpine glacier, *J. Geophys. Res.*, *109*, F03005, doi:10.1029/2004JF000120.

Aster, R., B. Borchers, and C. H. Thurber (2005), *Parameter Estimation and Inverse Problems*, Elsevier, Boston, Mass.

Bradford, J. H., J. Nichols, T. D. Mikesell, and J. T. Harper (2009), Continuous profiles of electromagnetic wave velocity and water content in glaciers: An example from Bench Glacier, Alaska, USA, *Ann. Glaciol.*, *50*(51), 1–9.

Cuffey, K. M., and W. S. B. Paterson (2010), *The Physics of Glaciers*, 4th ed., Eslevier, Burlington, Mass.

Deichmann, N., J. Ansorge, F. Scherbaum, A. Aschwanden, F. Bernardi, and G. Gudmundsson (2000), Evidence for deep icequakes in an alpine glacier, *Ann. Glaciol.*, *31*, 85–90.

Earle, P. S., and P. M. Shearer (1994), Characterization of global seismograms using an automatic-picking algorithm, *Bull. Seismol. Soc. Am.*, *84*(2), 366–376.

Ekstrom, G., M. Nettles, and V. C. Tsai (2006), Seasonality and increasing frequency of Greenland glacial earthquakes, *Science*, *311*(5768), 1756–1758, doi:10.1126/science.1122112.

Fudge, T. J., N. F. Humphrey, J. T. Harper, and W. T. Pfeffer (2008), Diurnal fluctuations in borehole water levels: Configuration of the drainage system beneath Bench Glacier, Alaska, USA, *J. Glaciol.*, *54*(185), 297–306.

Gammon, P. H., H. Kiefte, M. J. Clouter, and W. W. Denner (1983), Elastic constants of artificial and natural ice samples by Brillouin spectroscopy, *J. Glaciol.*, *29*(106), 433–460.

Geiger, L. (1910), Herdbestimmung bei Erdbeben aus den Ankunftszeiten, *Nachr. Königlichen Gese. Wiss. Göttingen*, *4*, 331–349.

Harper, J. T., N. F. Humphrey, and W. T. Pfeffer (1998), Crevasse patterns and the strain-rate tensor: A high resolution comparison, *J. Glaciol.*, *44*(146), 68–76.

Harper, J. T., N. F. Humphrey, W. T. Pfeffer, and B. Lazar (2007), Two modes of accelerated glacier sliding related to water, *Geophys. Res. Lett.*, *34*, L12503, doi:10.1029/2007GL030233.

Howat, I. M., I. Joughin, and T. A. Scambos (2007), Rapid changes in ice discharge from Greenland outlet glaciers, *Science*, *315*(5818), 1559–1561, doi:10.1126/science.1138478.

Jacobs, S. S., H. H. Helmer, C. S. M. Doake, A. Jenkins, and R. M. Frohlich (1992), Melting of ice shelves and the mass balance of Antarctica, *J. Glaciol.*, *38*(130), 375–387.

Lay, T., and T. C. Wallace (1995), *Modern Global Seismology*, Academic, San Diego, Calif.

Lin, F., M. H. Ritzwoller, and W. Shen (2011), On the reliability of attenuation measurements from ambient noise cross-correlations, *Geophys. Res. Lett.*, *38*, L11303, doi:10.1029/2011GL047366.

Meier, M. F., M. B. Dyurgerov, U. K. Rick, S. O'Neel, W. T. Pfeffer, R. S. Anderson, S. P. Anderson, and A. F. Glazovsky (2007), Glaciers dominate eustatic sea-level rise in the 21st century, *Science*, *317*(5841), 1064–1067, doi:10.1126/science.1143906.

Müller, G. (2001), Volume change of seismic sources from moment tensors, *Bull. Seismol. Soc. Am.*, *91*(4), 880–884.

Neave, K. G., and J. C. Savage (1970), Icequakes on the Athabasca Glacier, *J. Geophys. Res.*, *75*(8), 1351–1362.

O'Neel, S., H. P. Marshall, D. E. McNamara, and W. T. Pfeffer (2007), Seismic detection and analysis of icequakes at Columbia Glacier, Alaska, *J. Geophys. Res.*, *112*, F03S23, doi:10.1029/2006JF000595.

Peters, L. E., S. Anandakrishnan, R. B. Alley, and D. E. Voigt (2012), Seismic attenuation in englacial ice: A proxy for englacial temperature, *J. Geophys. Res.*, *117*, F02008, doi:10.1029/2011JF002201.

Petrenko, V. F., and R. W. Whitworth (2002), *Physics of Ice*, Oxford Univ. Press, New York.

Qamar, A. (1988), Calving icebergs: A source of low-frequency seismic signals from Columbia Glacier, Alaska, *J. Geophys. Res.*, *93*(B6), 6615–6623.

Rignot, E., and P. Kanagaratnam (2006), Changes in the velocity structure of the Greenland ice sheet, *Science*, *311*(5763), 986–990, doi:10.1126/science.1121381.

Roux, P.-F., F. Walter, P. Riesen, S. Sugiyama, and M. Funk (2010), Observation of surface seismic activity changes of an Alpine glacier during a glacier-dammed lake outburst, *J. Geophys. Res.*, *115*, F03014, doi:10.1029/2009JF001535.

Schaff, D. P., and G. C. Beroza (2004), Coseismic and postseismic velocity changes measured by repeating earthquakes, *J. Geophys. Res.*, *109*, B10302, doi:10.1029/2004JB003011.

Schaff, D. P., and P. G. Richards (2004), Repeating seismic events in China, *Science*, *303*(5661), 1176–1178, doi:10.1126/science.1093422.

Schaff, D. P., and P. G. Richards (2011), On finding and using repeating seismic events in and near China, *J. Geophys. Res.*, *116*, B03309, doi:10.1029/2010JB007895.

Smith, A. M. (2007), Subglacial bed properties from normal-incidence seismic reflection data, *J. Environ. Eng. Geophys.*, *12*(1), 3–13, doi:10.2113/JEEG12.1.3.

Stein, S., and M. Wysession (2003), *An Introduction to Seismology, Earthquakes, and Earth Structure*, Blackwell, Malden, Mass.

Stuart, G., T. Murray, A. Brisbourne, P. Styles, and S. Toon (2005), Seismic emissions from a surging glacier: Bakaninbreen, Svalbard, *Ann. Glaciol.*, *42*, 151–157, doi:10.3189/172756405781812538.

Truffer, M., and M. Fahnestock (2007), Climate change: Rethinking ice sheet time scales, *Science*, *315*(5818), 1508–1510, doi:10.1126/science.1140469.

Vidale, J. E. (1986), Complex polarization analysis of particle motion, *Bull. Seismol. Soc. Am.*, *76*(5), 1393–1405.

Waldhauser, F., and W. L. Ellsworth (2000), A double-difference earthquake location algorithm: Method and application to the Northern Hayward Fault, California, *Bull. Seismol. Soc. Am.*, *90*(6), 1353–1368.

Walter, F., N. Deichmann, and M. Funk (2008), Basal icequakes during changing subglacial water pressures beneath Gornergletscher, Switzerland, *J. Glaciol.*, *54*(186), 511–521.

Walter, F., J. F. Clinton, N. Deichmann, D. S. Dreger, S. E. Minson, and M. Funk (2009), Moment tensor inversions of icequakes on Gornergletscher, Switzerland, *Bull. Seismol. Soc. Am.*, *99*(2A), 852–870.

Walter, J. I., E. E. Brodsky, S. Tulaczyk, S. Y. Schwartz, and R. Pettersson (2011), Transient slip events from nearfield seismic and geodetic data on a glacier fault, Whillans Ice Plain, West Antarctica, *J. Geophys. Res.*, *116*, F01021, doi:10.1029/2010JF001754.

West, L., D. Rippin, T. Murray, H. Mader, and B. Hubbard (2007), Dielectric permittivity measurements on ice cores: Implications for interpretation of radar to yield glacial unfrozen water content, *J. Environ. Eng. Geophys.*, *12*, 37–45.

Wiens, D. A., S. Anandakrishnan, J. P. Winberry, and M. A. King (2008), Simultaneous teleseismic and geodetic observations of the stick–slip motion of an Antarctic ice stream, *Nature*, *453*(7196), 770–774, doi:10.1038/nature06990.

Yilmaz, O. (2001), *Seismic Data Analysis*, Soc. Explor. Geophys., Tulsa, Okla.